

The Nanoscale Free-Electron Model

D. F. Urban^{1,†}, J. Bürki², C. A. Stafford³, and
Hermann Grabert^{1,4}

¹Physikalisches Institut, Albert-Ludwigs-Universität, Hermann-Herder-Straße 3,
D-79104 Freiburg, Germany

²Department of Physics and Astronomy, California State University, 6000 J Street,
Sacramento, CA 95819-6041, USA

³Department of Physics, University of Arizona, 1118 E. Fourth Street, Tucson,
AZ 85721, USA

⁴Freiburg Institute for Advanced Studies, Albert-Ludwigs-Universität, Albertstraße
19, D-79104 Freiburg

[†]Email: urban@physik.uni-freiburg.de

Abstract. A brief review of the nanoscale free-electron model of metal nanowires is presented. This continuum description of metal nanostructures allows for a unified treatment of cohesive and conducting properties. Conductance channels act as delocalized chemical bonds whose breaking is responsible for jumps in the conductance and force oscillations. It is argued that surface and quantum-size effects are the two dominant factors in the energetics of a nanowire, and much of the phenomenology of nanowire stability and structural dynamics can be understood based on the interplay of these two competing factors. A linear stability analysis reveals a sequence of “magic” conductance values for which the underlying nanowire geometry is exceptionally stable. The stable configurations include Jahn-Teller deformed wires of broken axial symmetry. The model naturally explains the experimentally observed shell and supershell structures.

Contents

1	Introduction	2
2	Assumptions and limitations of the NFEM	4
3	Formalism of the NFEM	5
3.1	Scattering matrix formalism	5
3.2	WKB approximation	6
3.3	WKB approximation for non-axisymmetric wires	9
3.4	Weyl-expansion	9
3.5	Material dependence	10
4	Conductance and Force	11
4.1	Conductance	11
4.2	Force	12
5	Linear Stability Analysis	13
5.1	Rayleigh-Instability	14
5.2	Quantum-mechanical stability analysis	15
5.3	Axial symmetry	16
5.4	Breaking axial symmetry	17
5.5	General stability of cylinders	18
5.6	Comparison with experiments	19
5.7	Material dependence	21
6	Summary and discussion	22
7	References	23

1. Introduction

The past decades have seen an accelerating miniaturization of both mechanical and electrical devices, so that a better understanding of properties of ultrasmall systems is required in increasing detail. The first measurements of conductance quantization in the late 1980s (Wees *et al.* 1988, Wharam *et al.* 1988) in constrictions of two-dimensional electron gases formed by means of gates, have demonstrated the importance of quantum confinement effects in these systems and opened a wide field of research. A major step has been the discovery of conductance quantization in metallic nanocontacts (Agraït *et al.* 1993, Brandbyge *et al.* 1995, Krans *et al.* 1995): The conductance measured during the elongation of a metal nanowire is a steplike function where the typical step height is frequently near a multiple of the conductance quantum $G_0 = 2e^2/h$, where e is the electron charge and h Planck's constant. Surprisingly, this was initially not interpreted as a quantum effect but rather as a consequence of abrupt atomic rearrangements and elastic deformation stages. This interpretation, supported by a series of molecular dynamics simulations (Landman *et al.* 1990, Todorov *et al.* 1993), was claimed to be confirmed by another pioneering experiment (Rubio *et al.* 1996, Stalder *et al.* 1996) measuring simultaneously the conductance and the cohesive force of gold nanowires with diameters ranging from several Ångströms to several nanometers. As the contact was pulled apart, oscillations in the force of order 1nN were observed in perfect correlation with the conductance steps.

It came as a surprise when Stafford *et al.* (1997) introduced the free-electron model of a nanocontact – referred to as the *Nanoscale Free-Electron Model* (NFEM) henceforth – and showed that this comparatively simple model, which emphasizes the quantum confinement effects of the metallic electrons, is able to reproduce quantitatively the main features of the experimental observations. In this approach, the nanowire is understood to act as a quantum waveguide for the conduction electrons (which are responsible for both conduction and cohesion in simple metals): Each quantized mode transmitted through the contact contributes G_0 to the conductance and a force of order E_F/λ_F to the cohesion, where E_F and λ_F are the Fermi energy and wavelength, respectively. Conductance channels act as delocalized bonds whose stretching and breaking is responsible for the observed force oscillations, thus explaining straightforwardly their correlations with the conductance steps.

Since then, free-standing metal nanowires, suspended from electrical contacts at their ends, have been fabricated by a number of different techniques. Metal wires down to a single atom thick were extruded using a scanning-tunneling microscope tip (Rubio *et al.* 1996, Untiedt *et al.* 1997). Metal nanobridges were shown to “self-assemble” under electron-beam irradiation of thin metal films (Kondo *et al.* 1997, 2000, Rodrigues *et al.* 2000), leading to nearly perfect cylinders down to four atoms in diameter, with lengths up to fifteen nanometers. In particular, the mechanically-

controllable break junction technique, introduced by Moreland and Ekin (1985) and refined by Ruitenbeek and coworkers (Muller *et al.* 1992), has allowed for systematic studies of nanowire properties for a variety of materials. For a survey see the review by Agraït *et al.* (2003).

A remarkable feature of metal nanowires is that they are stable at all. Most atoms in such a thin wire are at the surface, with small coordination numbers, so that *surface effects* play a key role in their energetics. Indeed, macroscopic arguments comparing the surface-induced stress to the yield strength indicate a minimum radius for solidity of order ten nanometers (Zhang *et al.* 2003). Below this critical radius and absent some other stabilizing mechanism, plastic flow would lead to a Rayleigh instability (Chandrasekhar 1981) breaking the wire apart into clusters. Already in the 19th century Plateau (1873) realized that this surface-tension-driven instability is unavoidable if cohesion is due solely to classical pairwise interactions between atoms. The experimental evidence accumulated over the past decade on the remarkable stability of nanowires considerably thinner than the above estimate clearly shows that electronic effects emphasized by the NFEM dominate over atomistic effects for sufficiently small radii.

A series of experiments on alkali metal nanocontacts (Yanson *et al.* 1999, 2001) identified *electron-shell effects*, which represent the semiclassical limit of the quantum-size effects discussed above, as a key mechanism influencing nanowire stability. Energetically-favorable structures were revealed as peaks in conductance histograms, periodic in the nanowire radius, analogous to the electron-shell structure previously observed in metal clusters (de Heer 1993). A supershell structure was also observed (Yanson *et al.* 2000), in the form of a periodic modulation of the peak heights. More recently, such electron-shell effects have also been observed, even at room temperature, for the noble metals gold, copper, and silver (Diaz *et al.* 2003, Mares *et al.* 2004, 2005) as well as for aluminum (Mares *et al.* 2007).

Soon after the first experimental evidence for electron shell effects in metal nanowires, a theoretical analysis using the NFEM found that nanowire stability can be explained by a competition of the two key factors, surface tension and electron-shell effects (Kassubek *et al.* 2001). Both linear (Zhang *et al.* 2003, Urban *et al.* 2003) and nonlinear (Bürki *et al.* 2003, 2005a) stability analyses of axially symmetric nanowires found that the surface-tension driven instability can be completely suppressed in the vicinity of certain “magic radii.” However, the restriction to axial symmetry implies characteristic gaps in the sequence of stable nanowires, which is not fully consistent with the experimentally observed nearly perfect periodicity of the conductance peak positions. A Jahn-Teller deformation breaking the symmetry can lead to more stable deformed configurations. Recently, the linear stability analysis was extended to wires with arbitrary cross-section (Urban *et al.* 2004a, 2006). This general analysis confirms the existence of a sequence of magic cylindrical wires of exceptional stability which

represent roughly 75% of the main structures observed in conductance histograms. The remaining 25% are deformed and predominantly of elliptical or quadrupolar shapes. This result allows for a consistent interpretation of experimental conductance histograms for alkali and noble metals, including both the electronic shell and supershell structures (Urban *et al.* 2004b).

This chapter is intended to give an introduction to the NFEM. Section 2 summarizes the assumptions and features of the model while the general formalism is described in Sec. 3. In the following sections, two applications of the NFEM will be discussed: First, we give a unified explanation of electrical transport and cohesion in metal nanocontacts (Sec. 4) and second, the linear stability analysis for straight metal nanowires will be presented (Sec. 5). The latter will include cylindrical wires as well as wires with broken axial symmetry, thereby discussing the Jahn-Teller-effect.

2. Assumptions and limitations of the NFEM

Guided by the importance of conduction electrons in the cohesion of metals, and by the success of the jellium model in describing metal clusters (de Heer 1993, Brack 1993), the NFEM replaces the metal ions by a uniform, positively charged background that provides a confining potential for the electrons. The electron motion is free along the wire, and confined in the transverse directions. Usually an infinite confinement potential (hard-wall boundary conditions) for the electrons is chosen. This is motivated by the fact that the effective potential confining the electrons to the wire will be short ranged due to the strong screening in good metals.

In a first approximation electron-electron interactions are neglected, which is reasonable due to the excellent screening (Kassubek *et al.* 1999) in metal wires with $G > G_0$. It is known from cluster physics that a free electron model gives qualitative agreement and certainly describes the essential physics involved. Interaction, exchange and correlation effects as well as a realistic confinement potential have to be taken into account, however, for quantitative agreement.¹ From this we infer that the same is true for metal nanowires, where similar confinement effects are important. Remarkably, the electron-shell effects crucial to the stabilization of long wires are described with quantitative accuracy by the simple free-electron model, as discussed below.

In addition, the NFEM assumes that the positive background behaves like an incompressible fluid when deforming the nanowire. This takes into account, to lowest order, the hard-core repulsion of core electrons as well as the exchange energy of conduction electrons. When using a hard-wall confinement, the Fermi energy E_F (or equivalently the Fermi wavelength λ_F) is the only parameter entering the NFEM. As E_F is material dependent and experimentally accessible, there is no adjustable parameter.

¹ Note however, that the error introduced by using hard-walls instead of a more realistic soft-wall confining potential can be essentially corrected for by placing the hard-wall a finite distance outside the wire surface, thus compensating for the over-confinement (García-Martin *et al.* 1996).

This pleasant feature needs to be abandoned in order to model different materials more realistically. Different kinds of appropriate surface boundary conditions are imaginable in order to model the behaviour of an incompressible fluid and to fit the surface properties of various metals. This will be discussed in detail in Sec. 3.5.

A more refined model of a nanocontact would consider effects of scattering from disorder (Bürki *et al.* 1999a, b) and electron-electron interaction via a Hartree approximation (Stafford *et al.* 2000a, Zhang *et al.* 2005). The inclusion of disorder in particular leads to a better quantitative agreement with transport measurements, but does not change the cohesive properties qualitatively in any significant way, while electron-electron interactions are found to be a small correction in most cases. As a result, efforts to make the NFEM more realistic do not improve it significantly, while removing one of its main strengths, the absence of any adjustable parameters.

The major shortcoming of the NFEM is that its applicability is limited to good metals having a nearly spherical Fermi surface. It is best suited for the (highly reactive) s-orbital alkali metals, providing a theoretical understanding of the important physics in nanowires. The NFEM has also been proven to qualitatively (and often semi-quantitatively) describe noble metal nanowires, and in particular, gold. Lately, it has been shown that the NFEM can even be applied (within a certain parameter range) to describe the multivalent metal aluminum, since Al shows an almost spherical Fermi surface in the extended-zone scheme. The NFEM is especially suitable to describe shell effects due to the conduction-band s-electrons, and the experimental observation of a crossover from atomic-shell to electron-shell effects with decreasing radius in both metal clusters (Martin 1996) and nanowires (Yanson *et al.* 2001) justifies *a posteriori* the use of the NFEM in the later regime. Naturally, the NFEM does not capture effects originating from the directionality of bonding, such as the effect of surface reconstruction observed for Au. For this reason it cannot be used to model atomic chains of Au atoms, which are currently extensively studied experimentally. Keeping these limitations in mind, the NFEM is applicable within a certain range of radius, capturing nanowires with only very few atoms in cross-section up to wires of several nanometers in thickness, depending on the material under consideration.

3. Formalism of the NFEM

3.1. Scattering matrix formalism

A metal nanowire represents an open system connected to metallic electrodes at each end. These macroscopic electrodes act as ideal electron reservoirs in thermal equilibrium with a well-defined temperature and chemical potential. When treating an open system, the Schrödinger equation is most naturally formulated as a scattering problem. The basic idea of the scattering approach is to relate physical properties of the wire with

transmission and reflection amplitudes for electrons being injected from the leads.²

The fundamental quantity describing the properties of the system is the energy-dependent unitary scattering matrix $S(E)$ connecting incoming and outgoing asymptotic states of conduction electrons in the electrodes. For a quantum wire, $S(E)$ can be decomposed into four submatrices $S_{\alpha\beta}(E)$, $\alpha, \beta = 1, 2$, where 1 (2) indicates the left (right) lead. Each submatrix $S_{\alpha\beta}(E)$ determines how an incoming eigenmode of lead β is scattered into a linear combination of outgoing eigenmodes of lead α . The eigenmodes of the leads are also referred to as scattering channels.

The formulation of electrical transport in terms of the scattering matrix was developed by Landauer and Büttiker: The (linear response) electrical conductance G can be expressed as a function of the submatrix S_{21} which describes transmission from the source electrode 1 to the drain electrode 2 and is given by (Datta 1995)

$$G = \frac{2e^2}{h} \int dE \frac{-\partial f(E)}{\partial E} \text{Tr}_1 \left\{ S_{21}^\dagger(E) S_{21}(E) \right\}. \quad (1)$$

Here $f(E) = \{\exp[\beta(E - \mu)] + 1\}^{-1}$ is the Fermi distribution function for electrons in the reservoirs, $\beta = (k_B T)^{-1}$ is the inverse temperature and μ is the electron chemical potential, specified by the macroscopic electrodes. The trace Tr_1 sums over all eigenmodes of the source.

The appropriate thermodynamic potential to describe the energetics of an open system is the grand canonical potential

$$\Omega = -\frac{1}{\beta} \int dE D(E) \ln[1 + e^{-\beta(E-\mu)}], \quad (2)$$

where $D(E)$ is the electronic density of states (DOS) of the nanowire. Notably, the DOS of an open system may also be expressed in terms of the scattering matrix as (Dashen *et al.* 1969)

$$D(E) = \frac{1}{2\pi i} \text{Tr} \left\{ S^\dagger(E) \frac{\partial S}{\partial E} - \frac{\partial S^\dagger}{\partial E} S(E) \right\}, \quad (3)$$

where Tr sums over the states of both electrodes. This formula is also known as Wigner delay. Note that Eqs. (1), (2), and (3) include a factor of 2 for spin degeneracy.

Thus, once the electronic scattering problem for the nanowire is solved, both transport and energetic quantities can be readily calculated.

3.2. WKB approximation

For an axially symmetric constriction aligned along the z -axis, as depicted in Fig. 1, its geometry is characterized by the z -dependent radius $R(z)$. Outside the constriction, the solutions of the Schrödinger equation decompose into plane waves along the wire

² Phase-coherence is assumed to be preserved in the wire (a good approximation given the size of the system compared to the inelastic mean-free-path) and inelastic scattering is restricted to the electron reservoirs only.

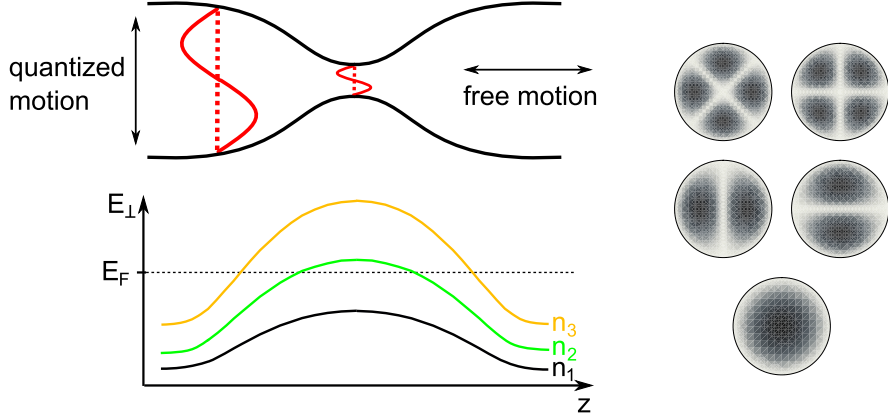


Figure 1. Upper-left part: Sketch of a nano-constriction. Within the adiabatic approximation, transverse and longitudinal motions are separable: the motion in the transverse direction is quantized, while in the longitudinal direction the electrons move in a potential created by the transverse energies [see Eq. (6)]. Lower-left part: Sketch of transverse energies for different transverse channels n_1 , n_2 , and n_3 as a function of the z -coordinate. Channel n_1 is transmitted through the constriction as its maximum transverse energy is smaller than the Fermi energy, channel n_2 is partly transmitted, and channel n_3 is almost totally reflected. Right part: Density plots of $|\Psi_n(r, \phi)|^2$ for the three eigenmodes depicted on the lower-left part, corresponding to five states due to degeneracies of energies E_{n_2} and E_{n_3} .

and discrete eigenmodes of a circular billiard in transverse direction. The eigenenergies $E_{\mu\nu}$ of a circular billiard are given by

$$E_{\mu\nu} = \frac{\hbar^2}{2m_e} \frac{\gamma_{\mu\nu}^2}{R_0^2}, \quad (4)$$

where the quantum number $\gamma_{\mu\nu}$ is the ν -th root of the Bessel function \mathcal{J}_μ of order μ and R_0 is the radius of the wire outside the constriction. In cylindrical coordinates r , φ , and z , the asymptotic scattering states read

$$\Psi_{\mu\nu}(r, \varphi, z) \sim e^{\pm i k_{\mu\nu} z + i \mu \varphi} \mathcal{J}_\mu(\gamma_{\mu\nu} r / R_0), \quad (5)$$

where $k_{\mu\nu}(E) = \sqrt{2m_e(E - E_{\mu\nu})/\hbar^2}$ is the longitudinal wavevector. In the following, we use multi-indices $n = (\mu\nu)$ in order to simplify the notation.

If the constriction is smooth, i.e. $|\partial R / \partial z| \ll 1$, one may use an adiabatic approximation. In the adiabatic limit, the transverse motion is separable from the motion parallel to the z -axis even in the region of the constriction, and the channel index n of an incoming electron is preserved throughout the wire. Accordingly, Eqs. (4) and (5) remain valid in the region of the constriction, with R_0 replaced by $R(z)$. The channel energies become functions of z , $E_n(z) = \hbar^2 \gamma_n^2 / 2m_e R(z)^2$, as is sketched in the lower part of Fig. 1, and act as a potential barrier for the effective one-dimensional scattering problem in channel n . The corresponding Schrödinger equation for the longitudinal part

Φ of the wave function reads

$$\frac{\partial^2}{\partial z^2} \Phi_n(z) + \frac{2m_e}{\hbar^2} [E - E_n(z)] \Phi_n(z) = 0, \quad (6)$$

and is solved within the WKB approximation (see, e.g., (Messiah 1999)) by

$$\Phi_n(r, \varphi, z) \sim \frac{1}{\sqrt{k_n(E, z)}} \exp \left[\pm i \int_0^z k_n(E, z') dz' \right]. \quad (7)$$

For a constriction of length L the transmission amplitude in channel n is then given by the familiar WKB barrier transmission factor

$$t_n(E) = \exp \left[i \int_0^L dz k_n(E, z) \right] \equiv \sqrt{\mathcal{T}_n(E)} e^{i\Theta_n(E)}. \quad (8)$$

Here \mathcal{T}_n is the transmission coefficient of channel n and Θ_n is the corresponding phase shift. The transmission amplitude gets exponentially damped in regions where the transverse energy is larger than the state total energy.³

The full S-matrix is now found to be of the form

$$S = \begin{pmatrix} i\sqrt{1-\mathcal{T}} e^{i\Theta} & \sqrt{\mathcal{T}} e^{i\Theta} \\ \sqrt{\mathcal{T}} e^{i\Theta} & i\sqrt{1-\mathcal{T}} e^{i\Theta} \end{pmatrix}, \quad (9)$$

where for simplicity of notation we have suppressed the channel indices and each of the entries is understood to be a diagonal matrix in the channels. Using the formulas of Sec. 3.1, we may proceed to determine physical quantities. From Eq. (1) we deduce that the electrical conductance at zero temperature reads,

$$\begin{aligned} G &= \frac{2e^2}{h} \sum_n \mathcal{T}_n(E_F) \\ &= \frac{2e^2}{h} \sum_n \exp \left[-2 \int_0^L dz \theta(E_n(z) - E_F) \sqrt{\frac{2m_e}{\hbar^2} (E_n(z) - E_F)} \right], \end{aligned} \quad (10)$$

where the second line is obtained by using Eq. (8). Here $\theta(x)$ denotes the Heaviside step function ($\theta(x) = 1$ for $x > 0$, 0 otherwise.) The density of states is found to be connected with the phase shift Θ_n ,

$$D(E) = \frac{2}{\pi} \sum_n \frac{\partial \Theta_n(E)}{\partial E} \quad (11)$$

$$= \frac{1}{\pi} \sqrt{\frac{2m_e}{\hbar^2}} \sum_n \int_0^L dz \frac{\theta(E - E_n(z))}{\sqrt{E - E_n(z)}}. \quad (12)$$

From the DOS, one gets the grand canonical potential in the limit of zero temperature as

$$\Omega \xrightarrow{T \rightarrow 0} -\frac{8E_F}{3\lambda_F} \int_0^L dz \sum_n \theta(E_F - E_n(z)) \left(1 - \frac{E_n(z)}{E_F} \right)^{3/2} \quad (13)$$

which can then be used to calculate the tensile force and stability of the nanowire, as discussed in the following sections.

³ This simplest WKB treatment does not correctly describe above-barrier reflection; a better approximation including this effect is described by Brandbyge *et al.* (1995) and by Glazman *et al.* (1988).

3.3. WKB approximation for non-axisymmetric wires

The formalism presented in the previous subsection can be readily extended to non-axisymmetric wires. In general, the surface of the wire is given by the radius function $r = R(\varphi, z)$, which may be decomposed into a multipole expansion

$$R(\varphi, z) = \rho(z) \left\{ \sqrt{1 - \sum_m \frac{\lambda_m(z)^2}{2}} + \sum_m \lambda_m(z) \cos[m(\varphi - \varphi_m(z))] \right\}, \quad (14)$$

where the sums run over positive integers. The parameterization is chosen in such a way that $\pi\rho(z)^2$ is the cross-sectional area at position z . The parameter functions $\lambda_m(z)$ and $\varphi_m(z)$ compose a vector $\mathbf{\Lambda}(z)$, characterizing the cross-sectional shape of the wire.

The transverse problem at fixed longitudinal position z now takes the form

$$\left(\frac{\partial^2}{\partial r^2} + \frac{1}{r} \frac{\partial}{\partial r} + \frac{1}{r^2} \frac{\partial^2}{\partial \varphi^2} + \frac{2m_e}{\hbar^2} E_n(z) \right) \chi_n(r, \varphi; z) = 0, \quad (15)$$

with boundary condition $\chi_n(R(\varphi, z), \varphi; z) = 0$ for all $\varphi \in [0, 2\pi]$. This determines the transverse eigenenergies $E_n(z) = E_n(\rho(z), \mathbf{\Lambda}(z))$ which now depend on the cross-sectional shape through the boundary condition. With the cross-section parametrization (14), their dependence on geometry can be written as

$$E_n(\rho, \mathbf{\Lambda}) = \frac{\hbar^2}{2m_e} \left(\frac{\gamma_n(\mathbf{\Lambda})}{\rho} \right)^2, \quad (16)$$

where the shape-dependent functions $\gamma_n(\mathbf{\Lambda})$ remain to be determined. In general, and in particular for non-integrable cross-sections, this has to be done by solving Eq. (15) numerically (Urban *et al.* 2006).

The adiabatic approximation (long-wavelength limit) implies the decoupling of transverse and longitudinal motions. One starts with the ansatz $\Psi(r, \varphi, z) = \chi(r, \varphi; z)\Phi(z)$ and neglects all z -derivatives of the transverse wavefunction χ . Again one is left with a series of effective one-dimensional scattering problems (Eq. 6) for the longitudinal wave functions $\Phi_n(z)$, in which the transverse eigenenergies $E_n(\rho(z), \mathbf{\Lambda}(z))$ act as additional potentials for the motion along the wire. These scattering problems can again be solved using the WKB approximation and Eqs. (11) and (13) apply.

3.4. Weyl-expansion

Semiclassical approximations often give an intuitive picture of the important physics and, due to their simplicity, allow for a better understanding of some general features. A very early analysis of the density of eigenmodes of a cavity with reflecting walls goes back to Weyl (1911) who proposed an expression in terms of the volume and surface area of the cavity. His formula was later rigorously proved and further terms in the expansion were calculated. Quite generally, we can express any extensive thermodynamic quantity as the sum of such a semiclassical Weyl expansion, which depends on geometrical quantities such as the system volume \mathcal{V} , surface area \mathcal{S} , and integrated mean curvature \mathcal{C} , as well as

an oscillatory shell-correction due to quantum-size effects (Brack 1997). In particular, the grand-canonical potential (2) can be written as

$$\Omega = -\omega \mathcal{V} + \sigma_s \mathcal{S} - \gamma_s \mathcal{C} + \delta\Omega, \quad (17)$$

where the energy density ω , surface tension coefficient σ_s , and curvature energy γ_s are, in general, material- and temperature-dependent coefficients. On the other hand, the shell correction $\delta\Omega$ can be shown, based on very general arguments (Strutinsky 1968, Zhang *et al.* 2005), to be a single-particle effect, which is well described by the NFEM.

3.5. Material dependence

Within the NFEM there is only one parameter entering the calculation apart from the contact geometry: the Fermi energy E_F , which is material dependent and in general well known (see Tab. 1). Nevertheless, the energy cost of a deformation due to surface and curvature energy, which can vary significantly for different materials, plays a crucial role when determining the stability of a nanowire. Obviously, when working with a free-electron model, contributions of correlation and exchange energy are not included, while they are known to play an essential role in a correct treatment of the surface energy (Lang 1973). Using the NFEM *a priori* implies the macroscopic free energy density $\omega = 2E_F k_F^3 / 15\pi^2$, the macroscopic surface energy $\sigma_s = E_F k_F^2 / 16\pi$, and the macroscopic curvature energy $\gamma_s = 2E_F k_F / 9\pi^2$. When drawing conclusions for metals having surface tensions and curvature energies that are rather different from these values, one has to think of an appropriate way to include these material-specific properties in the calculation.

A convenient way of modeling the material properties without losing the pleasant features of the NFEM is via the implementation of an appropriate surface boundary condition. Any atom-conserving deformation of the structure is subject to a constraint of the form

$$\mathcal{N} \equiv k_F^3 \mathcal{V} - \eta_s k_F^2 \mathcal{S} + \eta_c k_F \mathcal{C} = \text{const.} \quad (18)$$

This constraint on deformations of the nanowire interpolates between incompressibility and electroneutrality as side conditions, that is between volume conservation ($\eta_s = \eta_c = 0$) and treating the semiclassical expectation value for the charge Q_{Weyl} (Brack 1997) as an invariant ($\eta_s = 3\pi/8$, $\eta_c = 1$).

The grand canonical potential of a free-electron gas confined within a given geometry by hard-wall boundaries, as given by Eq. (17), changes under a deformation by

$$\begin{aligned} \Delta\Omega &= -\omega \Delta\mathcal{V} + \sigma_s \Delta\mathcal{S} - \gamma_s \Delta\mathcal{C} + \Delta[\delta\Omega] \\ &= -\frac{\omega}{k_F^3} \Delta\mathcal{N} + \left(\sigma_s - \frac{\omega}{k_F} \eta_s\right) \Delta\mathcal{S} - \left(\gamma_s - \frac{\omega}{k_F^2} \eta_c\right) \Delta\mathcal{C} + \Delta[\delta\Omega], \end{aligned} \quad (19)$$

where the constraint (18) was used to eliminate \mathcal{V} . Now the prefactors of the change in surface $\Delta\mathcal{S}$ and the change in integrated mean curvature $\Delta\mathcal{C}$ can be identified as

Element	Li	Na	K	Cu	Ag	Au	Al
E_F [eV]	4.74	3.24	2.12	7.00	5.49	5.53	11.7
k_F [nm ⁻¹]	11.2	9.2	7.5	13.6	12.0	12.1	17.5
σ_s [meV/Å ²]	27.2	13.6	7.58	93.3	64.9	78.5	59.2
σ_s [$E_F k_F^2$]	0.0046	0.0050	0.0064	0.0072	0.0082	0.0097	0.0017
η_s	1.135	1.105	1.001	0.939	0.866	0.755	1.146
γ_s [meV/Å]	62.0	24.6	14.9	119	96.4	161	121
γ_s [$E_F k_F$]	0.0117	0.0082	0.0094	0.0125	0.0146	0.0240	0.0059
η_c	0.802	1.06	0.971	0.741	0.583	-0.111	1.229

Table 1. Material parameters (Ashcroft and Mermin 1976, Perdew *et al.* 1991) of several monovalent metals: Fermi energy E_F , Fermi wavevector k_F , surface tension σ_s , and curvature energy γ_s , along with the corresponding values of η_s and η_c . The last column gives the corresponding values for the multivalent metal Al (see discussion in Sec. 5.7.) Adapted from (Urban *et al.* 2006).

effective surface tension and curvature energy, respectively. They can be adjusted to fit a specific material's properties by an appropriate choice of the parameters η_s and η_c (see Tab. 1).

4. Conductance and Force

The formalism presented in the previous section can now be applied to a specific wire geometry (Stafford *et al.* 1997), namely a cosine constriction,

$$R(z) = \frac{R_0 + R_{min}}{2} + \frac{R_0 - R_{min}}{2} \cos\left(\frac{2\pi z}{L}\right), \quad (20)$$

of a cylindrical wire. One is interested in the mechanical properties of this metallic nanoconstriction in the regime of conductance quantization. The necessary condition to have well-defined conductance plateaus in a three-dimensional constriction was shown (Torres *et al.* 1994) to be $(\partial R / \partial z)^2 \ll 1$. In this limit, one may employ the adiabatic and WKB approximations and evaluate the expressions obtained in Sec. 3.2.

4.1. Conductance

The conductance is obtained from Eq. (10). As the transmission amplitudes \mathcal{T}_n vary exponentially from 1 to 0 when the transverse energy of the respective channel at the neck of the constriction traverses the Fermi energy, this results in a steplike behavior of the conductance with almost flat plateaus in between. This is the phenomenon of conductance quantization, which is observable even at room temperature for noble metal nanowires due to the large spacing of transverse energies (of order 1 eV for Au, to compare to $k_B T \simeq 10^{-3}$ eV at room temperature). The upper panel of Fig. 2(a) shows the conductance obtained with an improved variant of the WKB approximation

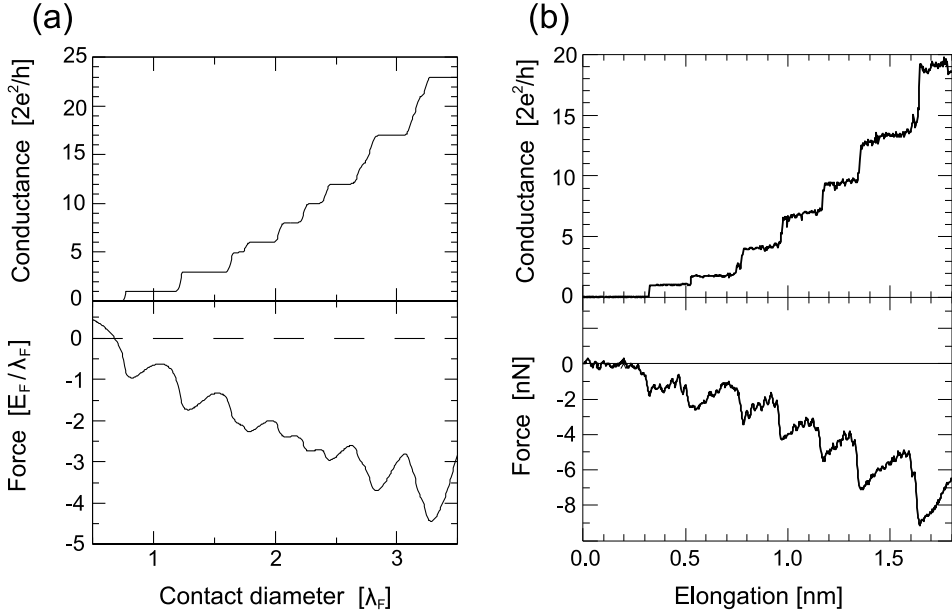


Figure 2. Electrical conductance G and tensile force F as function of elongation of a nanowire, (a) calculated in a WKB approximation for a cosine constriction (adapted from Stafford *et al.* 1997), and (b) measured by Rubio *et al.* (1996) in an experiment on gold (data courtesy of N. Agraït).

(Brandbyge *et al.* 1995, Glazman *et al.* 1988) for the geometry (20). The conductance as a function of elongation shows the expected steplike structure and the step heights are $2e^2/h$ and integer multiples thereof (the multiplicity depends on the degeneracy of the transverse modes). An ideal plastic deformation was assumed, i.e. the volume of the constriction was held constant during elongation.⁴

4.2. Force

If the wire elongation is slow enough, the electron gas has time to adjust to the wire shape changes during the deformation, and is thus always in equilibrium.⁵ Under these conditions, the tensile force can be computed from the grand canonical potential, given in the WKB approximation by Eq. (13), as $F = -\partial\Omega/\partial L|_{\mathcal{N}}$.

The lower panel of Fig. 2(a) shows the tensile force for the cosine constriction (20). The correlations between the force and conductance are striking: $|F|$ increases along the conductance plateaus, and decreases sharply when the conductance drops. The constriction becomes unstable when the last conductance channel is cut off, which is

⁴ Note the different abscissae for the theoretical and experimental graphs in Fig. 2. While both contact diameter and elongation are a measure of the deformation of the contact, the latter is more easily accessible to experiments. The contact diameter on the other hand is the natural independent geometric variable which is used for the theoretical graph, since its relation to elongation is very model-dependent.

⁵ The experimental elongation speed is of order 1nm/s, which is compatible with this assumption.

indicated by a positive tensile force. Some transverse channels are quite closely spaced, and in these cases, the individual conductance plateaus [e.g., $G/G_0 = 14, 15, 19, 21$] and force oscillations are difficult to resolve. The force oscillations are found to have an amplitude E_F/λ_F (i.e. ~ 1.7 nN for gold, consistent with experimental observations) independent of the chosen geometry (circular and quadratic wires and cosine and parabolic constrictions were tested), and to persist to very large conductances.

These results can be understood within the intuitive picture of a conductance channel as a delocalized metallic bond. The increase of $|F|$ along the conductance plateaus and the rapid decrease at the conductance steps can then be interpreted as stretching and breaking of these bonds. Note that within the NFEM, the correlation between conductance changes and force oscillations comes from a pure quantum-size effect and not from atomic rearrangements.

The comparison of theoretical predictions with experimental data by Rubio *et al.* (1996), plotted in Fig. 2(b), shows very good qualitative agreement and underlines that, although the NFEM is simple, it already gives a good qualitative description of the experimental findings. Extensions of the NFEM including structural dynamics of the wire (Bürki *et al.* 2003, 2007a,b), which are able to calculate the shape of the wire at all steps of elongation, find that instabilities accelerate the conductance and force jumps, making the theory even more similar to the experiment.

In addition, it is easy to show that in the NFEM, the tensile force is invariant under a stretching of the geometry $R(z) \rightarrow R(\lambda z)$, so that $F = (\varepsilon_F/\lambda_F) f(\Delta L/L_0, k_F R)$, where $f(x, y)$ is a dimensionless function, i.e. the force oscillations are universal, and thus do not depend on the details of the wire shape, or precisely how it deforms. Nonuniversal corrections to F occur in very short constrictions, for which the adiabatic approximation breaks down.

5. Linear Stability Analysis

Metal nanowires are of great interest for nanotechnology, since they may serve as conductors in future nanocircuits. In particular, one would like to know whether a nanowire of given length and radius remains stable at a given temperature.

At first sight, an atomistic approach seems to be more “realistic” than the NFEM and well suited to answer this question. But molecular dynamics (MD) simulations conceptually are not able to avoid the surface-tension-driven Rayleigh instability of long nanowires. Since quantum-size effects from the electron confinement are not properly taken into account, MD simulations fail to give an explanation for the electronic shell and supershell effects. On the other hand, atomistic quantum calculations using, e.g., the local-density approximation, are restricted to such small systems that their results can not really be disentangled from finite-size effects (Stafford *et al.* 2000b). Therefore, to date, a stability analysis within the framework of the NFEM (and generalizations thereof) is the only approach able to correctly include the effects of electron-shell filling

and thereby shed light on the puzzling stability of long metal nanowires.

The geometry of a wire of uniform cross section aligned along the z -axis is characterized by the cross-sectional area $\mathcal{A} = \pi\bar{\rho}^2$, and a set of dimensionless parameters determining the shape, which compose a vector $\bar{\mathbf{\Lambda}}$ (cf. Eq. 14). A small z -dependent perturbation of a wire of length L and initial cross section $(\bar{\rho}, \bar{\mathbf{\Lambda}})$ can be written in terms of a Fourier series as

$$\begin{aligned}\rho(z) &= \bar{\rho} + \varepsilon \delta\rho(z) = \bar{\rho} + \varepsilon \sum_q \rho_q e^{iqz}, \\ \mathbf{\Lambda}(z) &= \bar{\mathbf{\Lambda}} + \varepsilon \delta\mathbf{\Lambda}(z) = \bar{\mathbf{\Lambda}} + \varepsilon \sum_q \mathbf{\Lambda}_q e^{iqz},\end{aligned}\tag{21}$$

where the dimensionless small parameter ε sets the size of the perturbation.⁶

The energetic cost of a small deformation of the wire can be calculated by expanding the grand canonical potential as a series in the parameter ε ,

$$\Omega = \Omega^{(0)} + \varepsilon \Omega^{(1)} + \varepsilon^2 \Omega^{(2)} + \mathcal{O}(\varepsilon^3).\tag{22}$$

A nanowire with initial cross-section $(\bar{\rho}, \bar{\mathbf{\Lambda}})$ is energetically stable at temperature T if and only if $\Omega^{(1)}(\bar{\rho}, \bar{\mathbf{\Lambda}}, T) = 0$ and $\Omega^{(2)}(\bar{\rho}, \bar{\mathbf{\Lambda}}, T) > 0$ for every possible deformation $(\delta\rho, \delta\mathbf{\Lambda})$ satisfying the constraint (18).

5.1. Rayleigh-Instability

It is instructive to forget about quantum-size effects for a moment and to perform a stability analysis in the classical limit. For simplicity, one can restrict oneself to axial symmetry (i.e. $\mathbf{\Lambda} \equiv 0$). In the classical limit the grand canonical potential is given by the leading order terms of the Weyl approximation, $\Omega_{\text{Weyl}} = -\omega \mathcal{V} + \sigma_s \mathcal{S}$, and changes under the perturbation (21) by

$$\frac{\delta\Omega_{\text{Weyl}}}{L} = -2\pi(\bar{\rho}\omega - \sigma_s)\rho_0\varepsilon + \pi \sum_{q \neq 0} |\rho_q|^2 \left[-\omega + q^2 \bar{\rho} \sigma_s \right] \varepsilon^2.\tag{23}$$

Because of the constraint (18) on possible deformations, ρ_0 can be expressed in terms of the other Fourier coefficients. Volume conservation, e.g., implies $\rho_0 = -(\varepsilon/2\bar{\rho}) \sum_{q \neq 0} |\rho_q|^2$ and

$$\frac{\delta\Omega_{\text{Weyl}}(q)}{L} = \frac{\pi\sigma_s}{\bar{\rho}} \sum_{q \neq 0} |\rho_q|^2 (\bar{\rho}^2 q^2 - 1) \varepsilon^2\tag{24}$$

which has to be positive in order to ensure stability. Since q is restricted to integer multiples of $2\pi/L$, stability requires $L < 2\pi\bar{\rho}$. This is just the criterion of the classical Rayleigh instability (Chandrasekhar 1981): A wire longer than its circumference is unstable and likely to break up into clusters due to surface tension.

⁶ Assuming periodic boundary conditions, the perturbation wave vectors q must be integer multiples of $2\pi/L$. In order to ensure that $\rho(z)$ and $\mathbf{\Lambda}(z)$ are real, we have $\rho_{-q} = \rho_q^*$ and $\mathbf{\Lambda}_{-q} = \mathbf{\Lambda}_q^*$.

5.2. Quantum-mechanical stability analysis

The crucial ingredient to the stabilization of metal nanowires is the oscillatory shell correction $\delta\Omega$ to the grand canonical potential (17) which is due to quantum-size effects. This shell correction can be accounted for by a quantum-mechanical stability analysis based on the WKB-approximation introduced in Sec. 3.2. The use of this approximation can be justified *a posteriori* by a full quantum calculation (Urban *et al.* 2003, 2007) which shows that the structural stability of metal nanowires is indeed governed by their response to long-wavelength perturbations. The response to short-wavelength perturbations on the other hand controls a Peierls-type instability characterized by the opening of a gap in the electronic energy dispersion relation. This quantum mechanical instability, which is missing in the semiclassical WKB approximation, in fact limits the maximal length of stable nanowires. Nevertheless, if the wires are short enough, and/or the temperature is not too low, the full quantum calculation essentially confirms the semiclassical results.

A systematic expansion of Eq. (13) yields

$$\frac{\Omega^{(1)}}{L/\lambda_F} = 4 \sum_n \sqrt{\frac{E_F - \bar{E}_n}{E_F}} \left(\mathbf{\Lambda}_0 \cdot \bar{\mathbf{E}}'_n - 2\bar{E}_n \frac{\rho_0}{\bar{\rho}} \right), \quad (25)$$

$$\frac{\Omega^{(2)}}{L/\lambda_F} = E_F \sum_q \begin{pmatrix} \rho_q/\bar{\rho} \\ \mathbf{\Lambda}_q \end{pmatrix}^\dagger \begin{pmatrix} A_{\rho\rho} & A_{\rho\mathbf{\Lambda}} \\ A_{\mathbf{\Lambda}\rho} & A_{\mathbf{\Lambda}\mathbf{\Lambda}} \end{pmatrix} \begin{pmatrix} \rho_q/\bar{\rho} \\ \mathbf{\Lambda}_q \end{pmatrix}, \quad (26)$$

where the elements of the matrix A in Eq. (26) are given by

$$\begin{aligned} A_{\rho\rho} &= \sum_n \frac{4\bar{E}_n}{E_F^{3/2}} \left[3\sqrt{E_F - \bar{E}_n} - \frac{\bar{E}_n}{\sqrt{E_F - \bar{E}_n}} \right], \\ A_{\mathbf{\Lambda}\rho} &= - \sum_n \frac{4\bar{\mathbf{E}}'_n}{E_F^{3/2}} \left[\sqrt{E_F - \bar{E}_n} - \frac{\bar{E}_n}{2\sqrt{E_F - \bar{E}_n}} \right], \\ A_{\mathbf{\Lambda}\mathbf{\Lambda}} &= \sum_n \frac{1}{E_F^{3/2}} \left[2\bar{\mathbf{E}}''_n \sqrt{E_F - \bar{E}_n} - \frac{\bar{\mathbf{E}}'_n \cdot (\bar{\mathbf{E}}'_n)^\dagger}{\sqrt{E_F - \bar{E}_n}} \right]. \end{aligned} \quad (27)$$

Here $\bar{\mathbf{E}}'_n$ denotes the gradient of E_n with respect to $\mathbf{\Lambda}$ and $\bar{\mathbf{E}}''_n$ is the matrix of second derivatives. The bar indicates evaluation at $(\bar{\rho}, \bar{\mathbf{\Lambda}})$.

The number of independent Fourier coefficients in Eq. (21) is restricted through the constraint (18) on allowed deformations. Hence, after evaluating the change of the geometric quantities \mathcal{V} , \mathcal{S} , and \mathcal{C} due to the deformation, we can use Eq. (18) to express ρ_0 in terms of the other Fourier coefficients, yielding an expansion $\rho_0 = \rho_0^{(0)} + \varepsilon \rho_0^{(1)} + \mathcal{O}(\varepsilon^2)$. This expansion then needs to be inserted in Eqs. (25) and (26), thereby modifying the first-order change of the energy $\Omega^{(1)}$ and the stability matrix A (Urban *et al.* 2006).

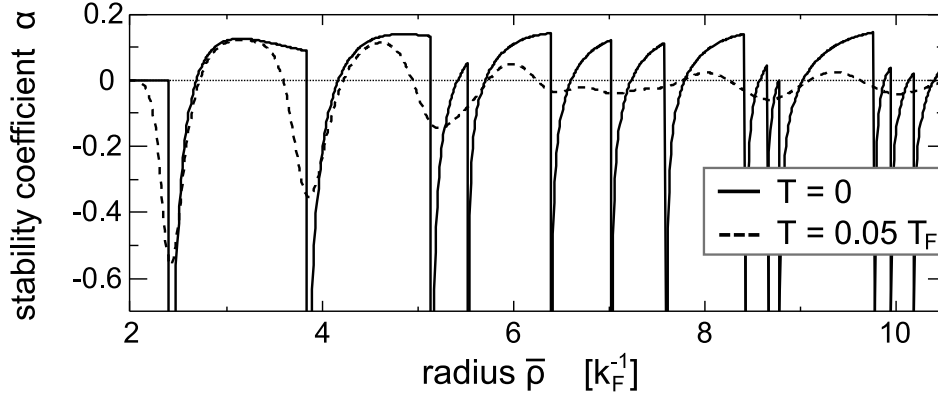


Figure 3. WKB stability coefficient, calculated using a constant-volume constraint. The sharp negative peaks at the opening of new channels (i.e. when $k_F \bar{\rho} = \gamma_n$) are smeared out with increasing temperature T .

Stability requires that the resulting modified stability matrix \tilde{A} be positive definite. Results at finite temperature are obtained essentially in a similar fashion, by integrating Eq. (2) numerically.

5.3. Axial symmetry

A straightforward application of the method outlined above is the stability analysis of cylindrical wires with respect to axisymmetric volume conserving perturbations. In this specific case $\Lambda(z) \equiv 0$ and $\rho_0 = -(\varepsilon/2\bar{\rho}) \sum_{q \neq 0} |\rho_q|^2$. Therefore, Eq. (25) takes the form $\Omega^{(1)} \equiv 0$ and Eq. (26) simplifies to read

$$\frac{\Omega^{(2)}}{L/\lambda_F} = E_F \sum_{q \neq 0} |\rho_q/\bar{\rho}|^2 \alpha(\bar{\rho}), \quad (28)$$

where the *stability coefficient* $\alpha(\bar{\rho}) \equiv \tilde{A}_{\rho\rho}$ reads (Urban *et al.* 2006)

$$\alpha(\bar{\rho}) = \sum_n \theta(k_F \bar{\rho} - \gamma_n) \frac{4\gamma_n^2}{(k_F \bar{\rho})^2} \left[4\sqrt{1 - \frac{\gamma_n^2}{(k_F \bar{\rho})^2}} - \frac{1}{\sqrt{(k_F \bar{\rho})^2 - \gamma_n^2}} \right]. \quad (29)$$

Axial symmetry implies the use of the transverse eigenenergies $E_n/E_F = (\gamma_n/k_F \bar{\rho})^2$, cf. Eq. (4). This result, valid for zero temperature, is plotted as a function of radius in Fig. 3 together with a numerical result at finite temperature. Sharp negative peaks at the subband thresholds, i.e. when $\bar{\rho} k_F = \gamma_n$, indicate strong instabilities whenever a new channel opens. On the other hand, α is positive in the regions between these thresholds giving rise to intervals of stability that decrease with increasing temperature. These islands of stability can be identified with the “magic radii” found in experiments. As will be shown below, one has to go beyond axial symmetry in order to give a full explanation of the observed conductance histograms of metal nanowires.

G/G_0	a	λ_2	T_{\max}/T_ρ
2	1.72	0.26	0.50
5	1.33	0.14	0.49
9	1.22	0.10	0.50
29	1.13	0.06	0.54
59	1.11	0.05	0.49
72	1.08	0.04	0.39
117	1.06	0.03	0.55
172	1.06	0.03	0.50

Table 2. Most stable deformed wires with quadrupolar cross sections. The first column gives the quantized conductance of the corresponding wire. Both the aspect ratio a and the value of the deformation parameter λ_2 are given. The maximum temperature of stability T_{\max} is given for each wire. In all cases the surface tension was set to 0.22 N/m, corresponding to Na. Adapted from (Urban *et al.* 2006).

5.4. Breaking axial symmetry

It is well known in the physics of crystals and molecules that a Jahn-Teller deformation breaking the symmetry of the system can be energetically favorable. In metal clusters, Jahn-Teller deformations are also very common, and most of the observed structures show a broken spherical symmetry. By analogy, it is natural to assume that for nanowires, too, a breaking of axial symmetry can be energetically favorable, and lead to more stable deformed geometries.

Canonical candidates for such stable non-axisymmetric wires are wires with a $\cos(m\varphi)$ -deformed cross section (i.e. having m -fold symmetry), a special case of Eq. (14) with only one non-zero λ_m . The quadrupolar deformation ($m = 2$) is expected to be the energetically most favorable of the multipole deformations⁷ since deformations with $m > 2$ become increasingly costly with increasing m , their surface energy scaling as m^2 .

The results of Sec. 5.2 can straightforwardly be used to determine stable quadrupolar configurations by intersection of the stationary curves, $\Omega^{(1)}(\bar{\rho}, \bar{\lambda}_2)|_{\mathcal{N}} = 0$, and the convex regions, $\Omega^{(2)}(\bar{\rho}, \bar{\lambda}_2)|_{\mathcal{N}} > 0$. The result is a so-called *stability diagram* which shows the stable geometries (at a given temperature) in configuration space, that is as a function of the geometric parameters $\bar{\rho}$ and $\bar{\lambda}_2$. An example of such a stability diagram is shown later in Fig. 6 for the case of aluminum, discussed in Sec. 5.7. Results for all temperatures can then be combined, thus adding a third axis (i.e. temperature) to the stability diagram. Finally, the most stable configurations can be extracted, defined as those geometries that persist up to the highest temperature compared to their neighboring configurations.

⁷ The dipole deformation ($m = 1$) corresponds, in leading order, to a simple translation, plus higher-order multipole deformations. Therefore the analysis can be restricted to $m > 1$.

Table 2 lists the most stable deformed sodium wires with quadrupolar cross section, obtained by the procedure described above. The deformation of the stable structures is characterized by the parameter λ_2 or equivalently by the aspect ratio

$$a = \frac{\sqrt{1 - \lambda_2^2/2} + \lambda_2}{\sqrt{1 - \lambda_2^2/2} - \lambda_2}. \quad (30)$$

Clearly, nanowires with highly-deformed cross sections are only stable at small conductance. The maximum temperature up to which the wires remain stable, given in the last column of Tab. 2, is expressed in units of $T_\rho := T_F/(k_F \bar{\rho})$. The use of this characteristic temperature reflects the temperature dependence of the shell correction to the wire energy (Urban *et al.* 2006).

Deformations with higher m cost more and more surface energy. Compared to the quadrupolar wires, the number of stable configurations with 3-, 4-, 5-, and 6-fold symmetry, their maximum temperature of stability, and their size of the deformations involved, all decrease rapidly with increasing order m of the deformation. For $m > 6$ no stable geometries are known. All this reflects the increase in surface energy with increasing order m of the deformation.

5.5. General stability of cylinders

It is possible to derive the complete stability diagram for cylinders, i.e., to determine the radii of cylindrical wires that are stable with respect to *arbitrary* small, long-wavelength deformations (Urban *et al.* 2006). At first sight, considering arbitrary deformations, and therefore theoretically an infinite number of perturbation parameters seems a formidable task. Fortunately, the stability matrix \tilde{A} for cylinders is found to be diagonal, and therefore the different Fourier contributions of the deformation decouple. This simplifies the problem considerably, since it allows to determine the stability of cylindrical wires with respect to arbitrary deformations through the study of a set of pure m -deformations, i.e. deformations as given by Eq. (14) with only one non-zero λ_m .

Figure 4 shows the stable cylindrical wires in dark gray as a function of temperature. The surface tension was fixed at the value for Na, see Tab. 1. The stability diagram was obtained by intersecting a set of individual stability diagrams allowing $\cos(m\varphi)$ -deformations with $m \leq 6$. This analysis confirms the extraordinary stability of a set of wires with so called “magic radii”. They exhibit conductance values $G/G_0 = 1, 3, 6, 12, 17, 23, 34, 42, 51, \dots$. It is noteworthy that some wires that are stable at low temperatures when considering only axisymmetric perturbations, e.g., $G/G_0 = 5, 10, 14$, are found to be unstable when allowing more general, symmetry-breaking deformations.

The heights of the dominant stability peaks in Fig. 4 exhibit a periodic modulation, with minima occurring near $G/G_0 = 9, 29, 59, 117, \dots$. The positions of these minima are in perfect agreement with the observed supershell structure in conductance histograms of alkali metal nanowires (Yanson *et al.* 2000). Interestingly, the nodes of the supershell

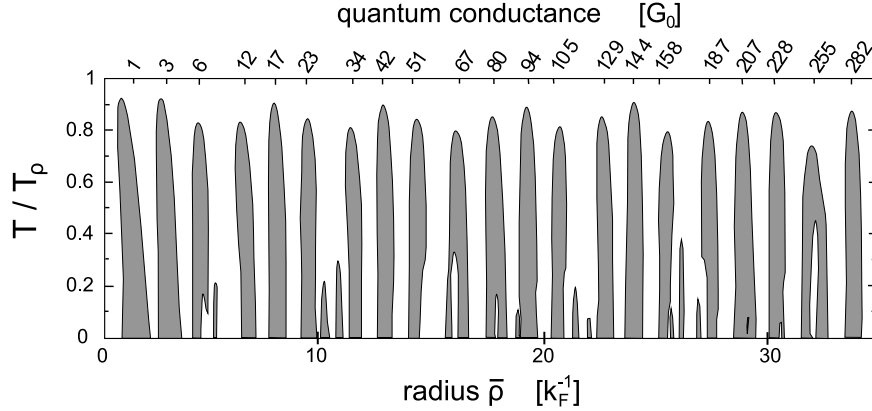


Figure 4. Stability of metal nanocylinders versus electrical conductance and temperature. Dark gray areas indicate stability with respect to arbitrary small deformations. Temperature is displayed in units of $T_\rho = T_F/k_F\bar{\rho}$ (see text). The surface tension was taken as 0.22 N/m, corresponding to Na. Adapted from (Urban *et al.* 2006).

structure, where the shell effect for a cylinder is suppressed, are precisely where the most stable deformed nanowires are predicted to occur (see discussion above). Thus symmetry breaking distortions and the supershell effect are inextricably linked.

Linear stability is a necessary—but not a sufficient—condition for a nanostructure to be observed experimentally. The linearly stable nanocylinders revealed in the above analysis are in fact *metastable* structures, and an analysis of their lifetime has been carried out within an axisymmetric stochastic field theory by Bürki *et al.* (2005a). There is a strong correlation between the height of the stable fingers in the linear stability analysis and the size of the activation barriers ΔE , which determines the nanowire lifetime τ through the Kramers formula $\tau = \tau_0 \exp(\Delta E/k_B T)$. This suggests that the linear stability analysis, with temperature expressed in units of $T_\rho = T_F/k_F\bar{\rho}$, provides a good measure of the total stability of metal nanowires. In particular, the “universal” stability of the most stable cylinders is reproduced, wherein the absolute stability of the magic cylinders is essentially independent of radius (aside from the small supershell oscillations).

5.6. Comparison with experiments

A detailed comparison between the theoretically most stable structures and experimental data for sodium is provided in Fig. 5. For each stable finger in the linear stability analysis its mean conductance is extracted and plotted as a function of its index number, together with experimental data by Yanson *et al.* (1999). This comparison shows that there is a one-to-one relation between observed conductance peaks and theoretically

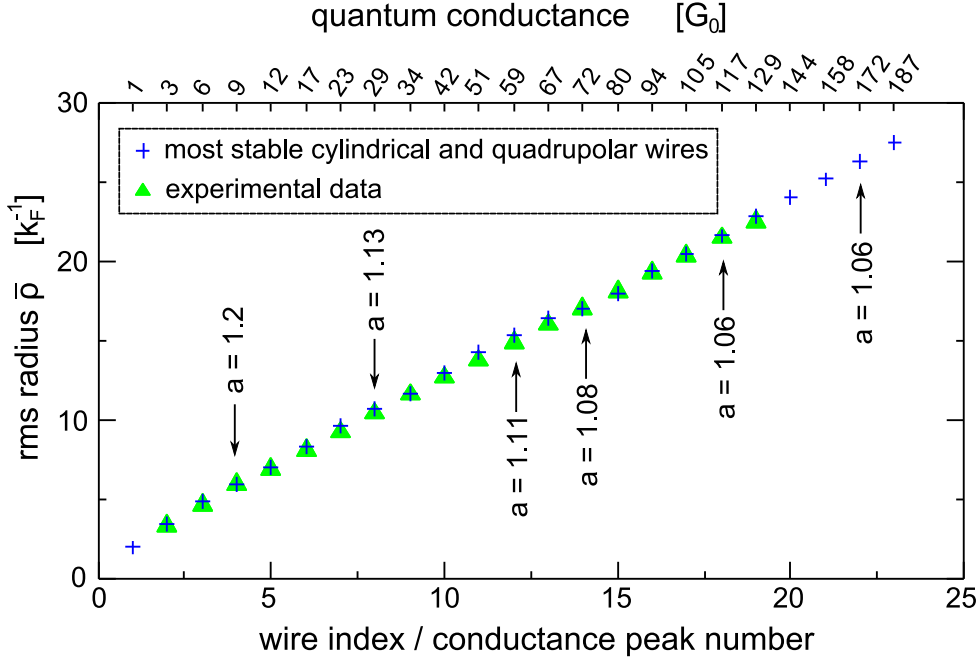


Figure 5. Comparison of the experimental shell structure for Na, taken from Yanson *et al.* (1999), with the theoretical predictions of the most stable Na nanowires. Non-axisymmetric wires are labeled with the corresponding aspect ratio a . Adapted from (Urban *et al.* 2004a).

stable geometries which in particular allows for a prediction of the cross-sectional shape of the wires. This striking fit is only possible when including non-axisymmetric wires, which represent roughly 25% of the most stable structures and which are labeled by the corresponding aspect ratios a in Fig. 5. The remaining 75% of the principal structures correspond to the magic cylinders. The role of symmetry in the stability of metal nanowires is thus fundamentally different from the case of atomic nuclei or metal clusters, where the vast majority of stable structures have broken symmetry. The crucial difference between the stability of metal nanowires and metal clusters is not the shell effect, which is similar in both cases, but rather the surface energy, which favors the sphere, but abhors the cylinder.

Besides the geometries entering the comparison above, the stability analysis also reveals two highly deformed quadrupolar nanowires with conductance values of $2 G_0$ and $5 G_0$, cf. Tab. 2. They are expected to appear more rarely due to their reduced stability relative to the neighboring peaks, and their large aspect ratio a that renders them rather isolated in configuration space.⁸ Nevertheless they can be identified by a detailed analysis of conductance histograms of the alkali metals (Urban *et al.* 2004b).

⁸ A nanowire produced by pulling apart an axisymmetric contact has a smaller probability to transform into a highly deformed configuration than into a neighboring cylindrical configuration.

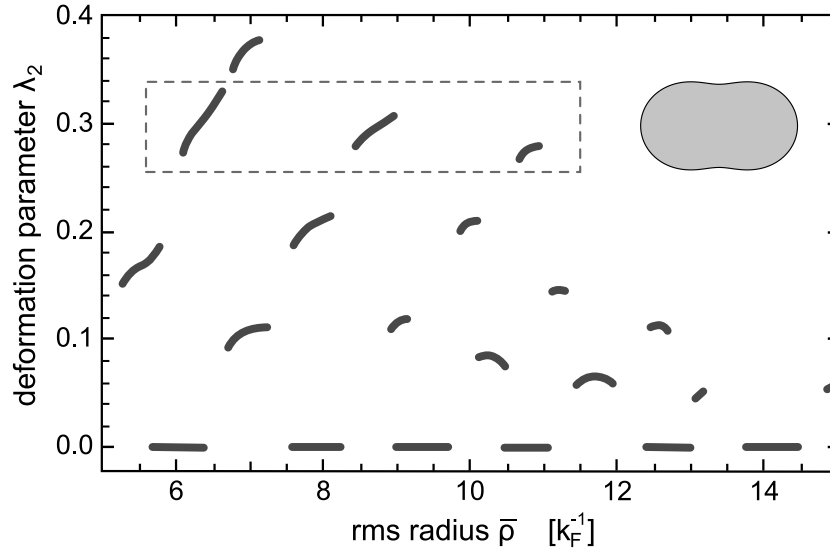


Figure 6. Stability diagram for Al wires at fixed temperature $T = 0.45 T_\rho$. Thick lines mark stable wires in the configuration space of rms radius $\bar{\rho}$ and deformation parameter λ_2 . The dashed box emphasizes a series of very stable superdeformed wires, whose peanut-shaped cross section is shown as an inset. This sequence was recently identified experimentally (Mares *et al.* 2007).

5.7. Material dependence

Results for different metals are similar in respect to the number of stable configurations and the conductance of the wires. On the other hand, the deviations from axial symmetry and the relative stability of Jahn-Teller deformed wires is sensitive to the material-specific surface tension and Fermi temperature. The relative stability of the highly deformed wires decreases with increasing surface tension $\sigma_s/(E_F k_F^2)$, measured in intrinsic units, and this decrease becomes stronger with increasing order m of the deformation. Therefore, for the simple s-orbital metals under consideration (Tab. 1), deformed Li wires have the highest, and Au wires have the lowest relative stability compared to cylinders of “magic radii.”⁹ Notable in this respect is Aluminum with $\sigma_s = 0.0017 E_F k_F^2$, some five times smaller than the value for Au. Aluminum is a trivalent metal, but the Fermi surface of bulk Al resembles a free-electron Fermi sphere in the extended-zone scheme. This suggests the applicability of the NFEM to Al nanowires, although the continuum approximation is more severe than for monovalent metals.

Recent experiments (Mares *et al.* 2007) have found evidence for the fact that the stability of aluminum nanowires also is governed by shell filling effects. Two magic series of stable structures have been observed with a crossover at $G \simeq 40 G_0$ and the exceptionally

⁹ Concerning the absolute stability, we have to consider that the lifetime of a metastable nanowire also depends on the surface tension (Bürki *et al.* 2005a).

stable structures have been related to electronic and atomic shell effects, respectively. Concerning the former, the NFEM can quantitatively explain the conductance and geometry of the stable structures for wires with $G > 12G_0$ and there is a perfect one-to-one correspondence of the predicted stable Al nanowires and the experimental electron-shell structure. Moreover, an experimentally observed third sequence of stable structures with conductance $G/G_0 \simeq 5, 14, 22$ provides intriguing evidence for the existence of “superdeformed” nanowires whose cross sections have an aspect ratio near 2:1. Theoretically, these wires are quite stable compared to other highly deformed structures and, more importantly, are very isolated in configuration space, as illustrated in the stability diagram shown in Fig. 6. This favors their experimental detection if the initial structure of the nanocontact formed in the break junction is rather planar with a large aspect ratio since then it is likely that the aspect ratio is maintained as the wire necks down elastically. Aluminum is unique in this respect and evidence of superdeformation has not been reported in any of the previous experiments on alkali and noble metals, presumably because highly-deformed structures are intrinsically less stable than nearly axisymmetric structures, due to their larger surface energy.

6. Summary and discussion

In this chapter we have given an overview on the Nanoscale Free-Electron Model, treating a metal nanowire as a non-interacting electron gas confined to a given geometry by hard-wall boundary conditions. At first sight, the NFEM seems to be an overly simple model, but closer study reveals that it contains very rich and complex features. Since its first introduction in 1997, it has repeatedly shown that it captures the important physics and is able to explain qualitatively, when not quantitatively, many of the experimentally observed properties of alkali and noble metal nanowires. Its strengths compared to other approaches are, in particular, the absence of any free parameters and the treatment of electrical and mechanical properties on an equal footing. Moreover, the advantage of obtaining analytical results allows the possibility to gain some detailed understanding of the underlying mechanisms governing the stability and structural dynamics of metal nanowires.

The NFEM correctly describes electronic quantum size effects, which play an essential role in the stability of nanowires. A linear stability analysis shows that the classical Rayleigh instability of a long wire under surface tension can be completely suppressed by electronic shell effects, leading to a sequence of certain stable “magic” wire geometries. The derived sequence of stable cylindrical and quadrupolar wires explains the experimentally observed shell and supershell structures for the alkali and noble metals as well as for aluminum. The most stable wires with broken axial symmetry are found at the nodes of the supershell structure, indicating that the Jahn-Teller distortions and the supershell effect are inextricably linked. In addition, a series of superdeformed aluminum nanowires with an aspect ratio near 2:1 is found which has lately been

identified experimentally. A more elaborate fully quantum mechanical analysis within the NFEM reveals an interplay between the Rayleigh and a Peierls-type instability. The latter is length-dependent and limits the maximal length of stable nanowires but other than that confirms the results obtained by the long wavelength expansion discussed above. Remarkably, certain gold nanowires are predicted to remain stable even at room temperature up to a maximal length in the micrometer range, sufficient for future nanotechnological applications.

The NFEM can be expanded by including the structural dynamics of the wire in terms of a continuum model of the surface diffusion of the ions. Furthermore, defects and structural fluctuations may also be accounted for. These extensions improve the agreement with experiments but do not alter the main conclusions. However, the NFEM does not address the discrete atomic structure of metal nanowires. With increasing thickness of the wire the effects of surface tension decrease and there is a crossover from plastic flow of ions to crystalline order, the latter implying atomic shell effects observed for thicker nanowires. Therefore, the NFEM applies to a window of conductance values between a few G_0 and about $100G_0$, depending on the material under consideration.

Promising extensions of the NFEM in view of current research activities are directed, e.g., towards the study of metal nanowires in nanoelectromechanical systems (NEMS) which couple nanoscale mechanical resonators to electronic devices of similar dimensions. The NFEM is ideally suited for the investigation of such systems since it naturally comprises electrical as well as mechanical properties. It is hoped that the generic behaviour of metal nanostructures elucidated by the NFEM can guide the exploration of more elaborate, material-specific models, in the same way that the free-electron model provides an important theoretical reference point from which to understand the complex properties of real bulk metals.

7. References

- Agraït, N., J. G. Rodrigo, and S. Vieira. 1993. Conductance steps and quantization in atomic-size contacts. *Phys. Rev. B* 47: 12345.
- Agraït, N., A. Levy Yeyati, and J. M. van Ruitenbeek. 2003. Quantum properties of atomic-sized conductors. *Phys. Rep.* 377: 81.
- Ashcroft, N. W. and N. D. Mermin. 1976. *Solid State Physics*. Saunders College Publishing.
- Brack, M. 1993. The physics of simple metal clusters: self-consistent jellium model and semiclassical approaches. *Rev. Mod. Phys.* 65: 677.
- Brack, M. and R. K. Bhaduri. 1997. *Semiclassical Physics*, volume 96 of *Frontiers in Physics*. Addison-Wesley, Reading, MA.
- Brandbyge, M., J. Schiøtz, M. R. Sørensen, *et al.* . 1995. Quantized conductance in atom-sized wires between two metals. *Phys. Rev. B* 52: 8499.
- Bürki, J., C. A. Stafford, X. Zotos, and D. Baeriswyl. 1999a. Cohesion and conductance of disordered metallic point contacts. *Phys. Rev. B* 60: 5000. *ibid.* *Phys. Rev. B* 62: 2956 (2000) (Erratum).
- Bürki, J. and C. A. Stafford. 1999b. Comment on "Quantum suppression of shot noise in atomic-size metallic contacts". *Phys. Rev. Lett.* 83: 3342.

- Bürki, J., R. E. Goldstein, and C. A. Stafford. 2003. Quantum necking in stressed metallic nanowires. *Phys. Rev. Lett.* 91: 254501.
- Bürki, J., C. A. Stafford, and D. L. Stein. 2005a. Theory of metastability in simple metal nanowires. *Phys. Rev. Lett.* 95: 090601.
- Bürki, J., and C. A. Stafford. 2005b. On the stability and structural dynamics of metal nanowires. *Appl. Phys. A* 81: 1519.
- Bürki, J. 2007a. Discrete thinning dynamics in a continuum model of metallic nanowires. *Phys. Rev. B* 75: 205435.
- Bürki, J. 2007b. Front propagation into unstable metal nanowires. *Phys. Rev. E* 76: 026317.
- Chandrasekhar, S. 1981. *Hydrodynamic and Hydromagnetic Stability*. Dover, New York.
- Dashen, R., S.-K. Ma, and H. J. Bernstein. 1969. S-matrix formulation of statistical mechanics. *Phys. Rev.* 187: 345.
- Datta, S. 1995. *Electronic Transport in Mesoscopic Systems*, 48–170. Cambridge University Press.
- de Heer, W. A. 1993. The physics of simple metal clusters: experimental aspects and simple models. *Rev. Mod. Phys.* 65: 611.
- Díaz, M., J. L. Costa-Krämer, E. Medina, A. Hasmy, and P. A. Serena. 2003. Evidence of shell structures in Au nanowires at room temperature. *Nanotechnology* 14: 113.
- García-Martin, A., J. A. Torres, and J. J. Sáenz. 1996. Finite size corrections to the conductance of ballistic wires. *Phys. Rev. B* 54: 13448.
- Glazman, L. I., G. B. Lesovik, D. E. Khmel'nitskii, and R. I. Shekter. 1988. Reflectionless quantum transport and fundamental ballistic-resistance steps in microscopic constrictions. *JETP Lett.* 48: 239.
- Kassubek, F., C. A. Stafford, and H. Grabert. 1999. Force, charge, and conductance of an ideal metallic nanowire. *Phys. Rev. B* 59: 7560.
- Kassubek, F., C. A. Stafford, H. Grabert, and R. E. Goldstein. 2001. Quantum suppression of the Rayleigh instability in nanowires. *Nonlinearity* 14: 167.
- Kondo, Y. and K. Takayanagi. 1997. Gold nanobridge stabilized by surface structure. *Phys. Rev. Lett.* 79: 3455.
- Kondo, Y. and K. Takayanagi. 2000. Synthesis and characterization of helical multi-shell gold nanowires. *Science* 289: 606.
- Krans, J. M., J. M. van Ruitenbeek, V. V. Fisun, I. K. Yanson, and L. J. de Jongh. 1995. The signature of conductance quantization in metallic point contacts. *Nature* 375: 767.
- Landman, U., W. D. Luedtke, N. A. Burnham, and R. J. Colton. 1990. Atomistic mechanisms and dynamics of adhesion, nanoindentation, and fracture. *Science* 248: 454.
- Lang, N. D. 1973. The density-functional formalism and the electronic structure of metal surfaces. *Solid State Phys.* 28: 225.
- Mares, A. I., A. F. Otte, L. G. Soukiassian, R. H. M. Smit, and J. M. van Ruitenbeek. 2004. Observation of electronic and atomic shell effects in gold nanowires. *Phys. Rev. B* 70: 073401.
- Mares, A. I. and J. M. van Ruitenbeek. 2005. Observation of shell effects in nanowires for the noble metals Cu, Ag, and Au. *Phys. Rev. B* 72: 205402.
- Mares, A. I., D. F. Urban, J. Bürki, H. Grabert, C. A. Stafford, and J. M. van Ruitenbeek. 2007. Electronic and atomic shell structure in aluminum nanowires. *Nanotechnology* 18: 265403.
- Martin, T. P. 1996. Shells of atoms. *Phys. Rep.* 273: 199.
- Messiah, A. 1999. *Quantum Mechanics*. Dover Pubs.
- Moreland, J. and J.W. Ekin. 1985. Electron tunneling experiments using Nb-Sn break junctions. *J. Appl. Phys.* 58: 3888.
- Muller, C. J., J. M. van Ruitenbeek, and L. J. de Jongh. 1992. Conductance and Supercurrent discontinuities in atomic-scale metallic constrictions of variable width. *Phys. Rev. Lett.* 69: 140.
- Perdew, J. P., Y. Wang, and E. Engel. 1991. Liquid-drop model for crystalline metals: Vacancy-formation, cohesive and face-dependent surface energies. *Phys. Rev. Lett.* 66: 508.

- Plateau, J. 1873. *Statique Expérimentale et Théorique des Liquides Soumis aux Seules Forces Moléculaires*. Gauthier-Villars, Paris.
- Rodrigues, V., T. Fuhrer, and D. Ugarte. 2000. Signature of atomic structure in the quantum conductance of gold nanowires. *Phys. Rev. Lett.* 85: 4124.
- Rubio, G., N. Agraït, and S. Vieira. 1996. Atomic-sized metallic contacts: mechanical properties and electronic transport. *Phys. Rev. Lett.* 76: 2302.
- Stafford, C. A., D. Baeriswyl, and J. Bürki. 1997. Jellium model of metallic nanocoherence. *Phys. Rev. Lett.* 79: 2863.
- Stafford, C. A., F. Kassubek, J. Bürki, H. Grabert, and D. Baeriswyl. 2000a. Cohesion, conductance, and charging effects in a metallic nanocontact, in *Quantum physics at the mesoscopic scale*, 49–53, EDP Sciences, Les Ulis, France.
- Stafford, C. A., J. Bürki, and D. Baeriswyl. 2000b. Comment on “Density functional simulation of a breaking nanowire”. *Phys. Rev. Lett.* 84: 2548.
- Stalder, A. and U. Dürig. 1996. Study of yielding mechanics in nanometer-sized Au contacts. *Appl. Phys. Lett.* 68: 637.
- Strutinsky, V. M. 1968. Shells in deformed nuclei. *Nucl. Phys. A* 122: 1.
- Todorov, T. N. and A. P. Sutton. 1993. Jumps in electronic conductance due to mechanical instabilities. *Phys. Rev. Lett.* 70: 2138.
- Torres, J. A., J. I. Pascual, and J. J. Sáenz. 1994. Theory of conduction through narrow constrictions in a three dimensional electron gas. *Phys. Rev. B* 49: 16581.
- Untiedt, C., G. Rubio, S. Vieira, and N. Agraït. 1997. Fabrication and characterization of metallic nanowires. *Phys. Rev. B* 56: 2154.
- Urban, D. F. and H. Grabert. 2003. Interplay of Rayleigh and Peierls instabilities in metallic nanowires. *Phys. Rev. Lett.* 91: 256803.
- Urban, D. F., J. Bürki, C. H. Zhang, C. A. Stafford, and H. Grabert. 2004a. Jahn-Teller distortions and the supershell effect in metal nanowires. *Phys. Rev. Lett.* 93: 186403.
- Urban, D. F., J. Bürki, A. I. Yanson, I. K. Yanson, C. A. Stafford, J. M. van Ruitenbeek, and H. Grabert. 2004b. Electronic shell effects and the stability of alkali nanowires. *Solid State Comm.* 131: 609.
- Urban, D. F., J. Bürki, C. A. Stafford, and H. Grabert. 2006. Stability and symmetry breaking in metal nanowires: The nanoscale free-electron model. *Phys. Rev. B* 74: 245414.
- Urban, D. F., C. A. Stafford, and H. Grabert. 2007. Scaling theory of the Peierls charge density wave in metal nanowires. *Phys. Rev. B* 75: 205428.
- van Wees, B. J., H. van Houten, C. W. J. Beenakker, *et al.* . 1988. Quantized conductance of point contacts in a two-dimensional electron gas. *Phys. Rev. Lett.* 60: 848.
- Weyl, H. 1911. Über die asymptotische Verteilung der Eigenwerte. *Nachr. akad. Wiss. Göttingen*, 110-117.
- Wharam, D. A., T. J. Thornton, R. Newbury, *et al.* . 1988. One-dimensional transport and the quantisation of the ballistic resistance. *J. Phys. C: Solid State Phys.* 21: L209.
- Yanson, A. I., I. K. Yanson, and J. M. van Ruitenbeek. 1999. Observation of shell structure in sodium nanowires. *Nature* 400: 144.
- Yanson, A. I., I. K. Yanson, and J. M. van Ruitenbeek. 2000. Supershell structure in alkali metal nanowires. *Phys. Rev. Lett.* 84: 5832.
- Yanson, A. I., I. K. Yanson, and J. M. van Ruitenbeek. 2001. Shell effects in alkali metal nanowires. *Fizika Nizkikh Temperatur* 27: 1092.
- Zhang, C. H., F. Kassubek, and C. A. Stafford. 2003. Surface fluctuations and the stability of metal nanowires. *Phys. Rev. B* 68: 165414.
- Zhang, C. H., J. Bürki, and C. A. Stafford. 2005. Stability of metal nanowires at ultrahigh current densities. *Phys. Rev. B* 71: 235404.